Title
Evaluating Materials Design Parameters of Hole-Selective Contacts for Silicon Heterojunction Solar Cells

Journal
IEEE Journal of Photovoltaics, 11(2)

ISSN
2156-3381

Authors
Woods-Robinson, Rachel
Fioretti, Angela N
Haschke, Jan
et al.

Publication Date
2021

DOI
10.1109/jphotov.2020.3038330

Peer reviewed

Evaluating Materials Design Parameters of Hole-Selective Contacts for Silicon Heterojunction Solar Cells

Rachel Woods-Robinson, *Graduate Student Member, IEEE*, Angela N. Fioretti, *Member, IEEE*, Jan Haschke, Mathieu Boccard, Kristin A. Persson, and Christophe Ballif, *Member, IEEE*

***Abstract*—Silicon heterojunction (SHJ) solar cell efficiencies are limited by parasitic absorption from the hydrogenated amorphous silicon (a-Si:H) front contact, but this may be mitigated by selecting an alternative carrier selective contact material with a wider band gap. When choosing such a material as the hole-selective contact ("p-layer"), the alignment of the material's valence band edge energy (E_{VB}) with that of crystalline silicon (c-Si) is an important criterion, but several other material parameters can also influence the band bending at the contact interface. In this article, we simulate an (n)c-Si/(i)a-Si:H/p-layer interface to explore the influence of six materials parameters in a variable p-layer on the SHJ performance. We find a strong influence on the fill factor (FF) from thickness, doping, and E_{VB}, and on V_{OC} from the interfacial defect density; notably, optimal E_{VB} is ∼0.1 eV higher than the valence band edge energy of a-Si:H. Multiparameter sensitivity analyses demonstrate how performance is simultaneously influenced by E_{VB} and doping; thus, both parameters should be optimized alongside one another. To assess the influence of these parameters experimentally, we grow p-type NiO_x as a test-case p-layer, which shows that FFs decrease with the oxygen content likely from the increased misalignment of E_{VB}. Although modest efficiencies are achieved experimentally (>7%), what is important is that our model simulates performance trends. With these results, we apply a materials discovery pipeline to suggest new materials (e.g., ZnTe and BeTe) to try as p-layers in the SHJ. This combination of simulations, experiments, and materials discovery informs a better understanding of contact selection in SHJ cells.**

I

I. Introduction

CLASSICAL, two-side contacted silicon heterojunction (SHJ) solar cells currently lag behind the power conversion efficiency of homojunctions and all-back contacted architectures due to parasitic absorption of short-wavelength light [1], [2]. In SHJ devices using an n-type wafer and a hole-selective contact stack on the front side, these challenges stem largely from this front contact stack, in which the typical requirements for an optimal contact stack—to be passivating, conductive, and carrier-selective [3]—are extended to also include broadband transparency. Despite research efforts to develop an alternative p-type contact with an improved transparency and carrier transport compared with standard p-doped amorphous silicon (p) a-Si:H, such as MoO_x [4]–[6] or doped microcrystalline silicon [7], [8], no SHJ cell based on these alternative contact materials has yet reached short-circuit current densities (J_{SC}) or front-surface transparencies comparable to the best front-homojunction designs. One material challenge is that a high-performing material that is both p-type conducting and transparent across the visible spectrum has not yet been discovered [9]–[12].

In recent years, computational materials design based on screening databases of electronic structure calculations has given rise to the ability to identify new compounds with desirable properties for specific optoelectronic applications [16]. Some of these screening efforts have resulted in publications listing novel p-type transparent materials that remain mostly unexplored in the experimental literature [17]–[20]. These materials represent an untapped resource of possible candidates for p-type carrier-selective contact applications; a situation that is largely due to the absence of a strong link between SHJ technology

This work was supported in part by the Swiss National Science Foundation under Ambizione Energy under Grant ICONS (PZENP2173627). The work of Rachel Woods-Robinson was supported in part by the NSF GRFP Graduate Fellowship (DGE1106400 and DGE1752814), in part by the U.C. Berkeley Chancellor's Fellowship, and in part by the ThinkSwiss Research Scholarship. The work of Angela N. Fioretti was supported by the Horizon 2020 Marie Skłodowska-Curie Actions under Grant 792720 (CLAReTE). The work of Kristin A. Persson was supported by the U.S. Department of Energy, Office of Science, Office of Basic Energy Sciences, Materials Sciences and Engineering Division under Contract DE-AC02-05CH11231 (Materials Project Program KC23MP). *(Corresponding author: Rachel Woods-Robinson.)*

Rachel Woods-Robinson and Kristin A. Persson are with the University of California and Lawrence Berkeley National Laboratory, Berkeley, CA 94720 USA (e-mail: rachelwoodsrobinson@gmail.com; kapersson@lbl.gov).

Mathieu Boccard and Christophe Ballif are with the Photovoltaics and Thin Film Electronics Laboratory, Institute of Microengineering, École Polytechnique Fédérale de Lausanne (EPFL), 2000 Neuchâtel, Switzerland (e-mail: mathieu.boccard@epfl.ch; christophe.ballif@epfl.ch).

Angela N. Fioretti was with the Photovoltaics and Thin Film Electronics Laboratory, Institute of Microengineering, École Polytechnique Fédérale de Lausanne (EPFL), 2000 Neuchâtel, Switzerland. He is now with Intel Corp., Hillsboro, OR USA (e-mail: angela.fioretti@epfl.ch).

Jan Haschke was with the Photovoltaics and Thin Film Electronics Laboratory, Institute of Microengineering, École Polytechnique Fédérale de Lausanne (EPFL), 2000 Neuchâtel, Switzerland. He is now with REC Solar Pte. Ltd., Singapore 637312, Singapore (e-mail: jan.haschke.pv@gmail.com).

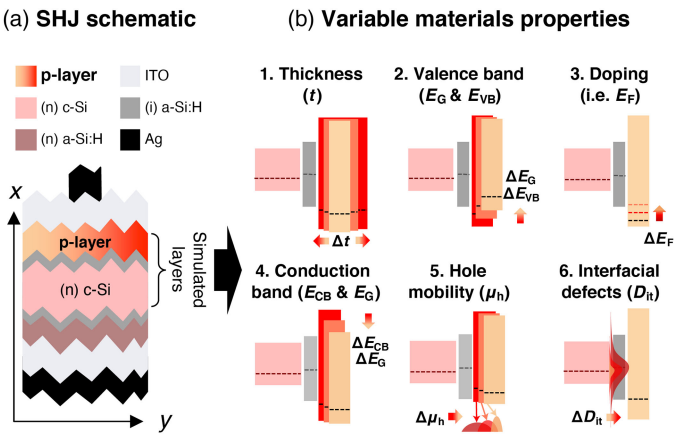

Fig. 1. (a) Silicon heterojunction (SHJ) solar cell device schematic. The "p-layer" is the hole-selective contact, and is depicted with an orange-red color gradient to represent the variability of properties explored in this study. (b) Graphical schematic of the six variable materials parameters of the p-type semitransparent hole-selective contact explored in this study. The three simulated layers are represented here: the pink rectangle is (n) c-Si, the gray rectangle is (i) a-Si:H, and the orange-red rectangles are the variable p-layer. The top and bottom edges of each rectangle are the conduction band edge and valence band edge, respectively, the dashed lines are the Fermi energies of each material, and the thick arrows represent an increasing value of a given property in the three different variable p-layer scenarios. The increased curvatures in the mobility schematic represent increased valence band edge dispersion (i.e., lower effective mass), and the D_{it} schematic represents a Gaussian-like distribution of interfacial defects.

and computational materials design. Such a link can be made for any given application by defining which material properties are most critical and determining their relevant ranges using targeted numerical simulations. The results can then be used to select candidate materials from the existing literature via computational screening.

In this work, we use 1-D numerical solar cell simulations to explore the impact of relevant hole-selective contact (i.e., "p-layer") material properties on the performance of a two-side contacted SHJ solar cell, as depicted in Fig. 1(a). These simulations allow the systematic tuning of one variable at a time or multiple variables simultaneously, as shown schematically in Fig. 1(b) with the orange-red color gradient, over a wide range that would otherwise be inaccessible experimentally. This approach allows us to assess the importance of each material parameter to the final solar cell performance and to elucidate the limits beyond which the power conversion efficiency decreases. The previous literature has assumed the valence band (VB) edge alignment to crystalline silicon (c-Si) as a principle design parameter; therefore, we select nickel oxide (NiO_x, with a VB edge energy $E_{\mathrm{VB,NiO}_x}$ close to that of c-Si, $E_{\mathrm{VB,c\text{-}Si}}$) as a test hole-selective contact material for both simulations and experiments in a full device stack. NiO_x has only rarely been studied as a hole-selective contact in SHJ solar cells [21], [22]. There are only a few reports of solar cell performance, and highest reported efficiencies up to 12.4% and open-circuit voltage (V_{OC}) values up to 510 mV [22]. Most notably, its tunable VB edge energy and facile growth conditions make it a suitable test material. The resulting insights are then used to guide new materials selection criteria, assess the tolerances of such criteria, and propose a list of as-yet underexplored materials suitable for application as hole-selective contacts in the SHJ architecture.

II. Methodology

A. Simulations and Calculations

Device modeling was performed using the AFORS-HET (automat for simulation of heterostructures) v2.5 1-D numerical simulation software [23], [24]. As depicted in the cell schematic in Fig. 1(a), we modeled the cell as a three-layer structure that consists of n-type crystalline silicon "(n) c-Si," intrinsic hydrogenated amorphous silicon "(i) a-Si:H," and the variable p-type hole-selective contact "p-layer." We assumed the other layers to be optimized, and thus excluded them and added flat-band Schottky interfaces at each side of the device stack. Table I reports the simulation parameters of each layer. Values for (n) c-Si and (i) a-Si:H are based on AFORS-HET standard layers [25]–[28] and "Standard (p) NiO_x" values are from the literature for a thin film with low hole doping (note that hole doping density can be much higher and many of these values are tunable, as we discuss subsequently) [13]–[15]. NiO_x is a test case for the variable p-layer, and the variable p-layer parameters were varied as depicted graphically in Fig. 1(b)—namely thickness, VB edge energy E_{VB} (i.e., negative ionization energy; we will define E_{VB} as a positive value herein), band gap E_{G}, hole doping concentration N_{A} (i.e., acceptor density, which determines the position of the Fermi level, E_{F}), hole mobility μ_{h}, and interfacial defect density D_{it}—within the range as reported in column "Variable p-layer." During variation of a single parameter, "Standard (p) NiO_x" values were used for all other parameters (except for E_{VB}, as discussed subsequently).

Effective interfacial defect density D_{it} was simulated using a common method from the literature [29], [30], which adds a thin 1-nm defective layer in between the (n) c-Si and (i) a-Si:H layers. This layer is a proxy for any interfacial defects that could occur between the modeled layers. As described in the "Defect layer" column of Table I, this layer has properties similar to c-Si, with continuous defects across the c-Si band gap. These defects were modeled as continuous donor-like (D) and acceptor-like (A) in the upper and lower halves of the band gap, respectively, and D_{it} was varied between 10^7 and 10^{17} $\mathrm{cm}^{-2}\mathrm{eV}^{-1}$. Electron and hole capture cross sections were set to 10^{-14} cm^2, as is conventional in AFORS-HET simulations that investigate D_{it} in various materials [29], [31]. Optical parameters in the AFORS-HET model were set to n and k values for silicon; we performed an uncertainty analysis using ellipsometry-derived optical parameters for NiO_x thin films [16], and observed no change in the performance.

For *ab initio* materials modeling of different compositions of NiO_x, NiO (mp-19009), and NiO_2 (mp-35925 and mp-25428) were selected from the Materials Project (MP) database as the end-point compounds of NiO_x ($1 < x < 2$). NiO is the rocksalt structure, with octahedral coordination of both Ni and O. NiO_2 (mp-35925) is a layered compound with octahedrally coordinated Ni atoms (while mp-25428 is a computationally predicted distorted derivative of the NiO rocksalt structure). Structures were relaxed using density functional theory (DFT),

TABLE I
AFORS-HET SIMULATION PARAMETERS FOR EACH MODELED LAYER

Layer	(n) c-Si	(i) a-Si:H	Variable p-layer	Standard (p) NiO_x*	Defect layer†
Thickness, t	180 μm	5 nm	0.1 – 300 nm	10 nm	1 nm
Band gap, E_G (eV)	1.124	1.72	1 – 4.5	3.2	1.124
CB edge energy, E_{CB} (eV)	4.05	3.9	1.5 – 2.75	1.8	4.05
VB edge energy, E_{VB} (eV)	5.17	5.62	5.1 – 5.9	5	5.17
Electron doping, N_D (cm^{-3})	1.56×10^{15}	1000	0	0	1.56×10^{15}
Hole doping, N_A (cm^{-3})	0	0	1×10^{10} – 1×10^{19}	5×10^{15}	0
Electron mobility, μ_e ($cm^2V^{-1}s^{-1}$)	1335	20	$3\mu_p$	0.326	1335
Hole mobility, μ_h ($cm^2V^{-1}s^{-1}$)	462.7	5	1×10^{-3} – 1×10^{3}	0.141	462.7
CB effective DOS, N_C (cm^{-3})	2.84×10^{19}	1×10^{21}	1×10^{20}	1×10^{20}	2.84×10^{19}
VB effective DOS, N_V (cm^{-3})	2.68×10^{19}	1×10^{21}	1×10^{20}	1×10^{20}	2.68×10^{19}
Dielectric constant, dk (-)	11.9	11.9	11.75	11.75	11.9
Defects (cm^{-2} eV^{-1})	single defect at $\frac{1}{2}E_G$	CB/VB tail, Gaussian A/D‡	—	—	continuous A/D‡: 10^7–10^{17}

*"Standard" values for a low p-type doped NiO_x [13]–[15].
†Interfacial defect layer modeled between (n) c-Si and (i) a-Si:H to simulate D_{it}.
‡"A/D" = acceptor and donor defects.

with the projector augmented wavefunction method [32], [33] as implemented in the Vienna *Ab Initio* Simulation Package [34], [35] within the Perdew–Berke–Ernzerhof (PBE) generalized gradient approximation (GGA) [36], and standard MP calculation parameters [37]. Branch point energy (BPE) calculations—which effectively average the CB and VB dispersion in a given material's computed band structure, assign an energy value based on this calculation, and then align this energy to that of another material to compare band edges—were used as a qualitative computational proxy for the band alignment [38]. The BPE values of NiO and NiO_2 were calculated using the Matminer (Materials Data Mining) simulation package [39], four VBs and two CBs were considered for the BPE calculations, and a sensitivity analysis was performed on various band consideration scenarios as outlined in the literature [16].

B. Solar Cell Fabrication and Characterization

Solar cells were fabricated on 195-μm-thick, textured, n-type float zone wafers with a resistivity of 2–3 Ωcm. Plasma-enhanced chemical vapor deposition was used to deposit $\sim$9 nm of hydrogenated intrinsic amorphous silicon (a-Si:H) on the front and back sides, followed by $\sim$30 nm of n-type doped a-Si:H as the electron-selective contact on the back. NiO_x layers were sputter-deposited on the front to uniform thicknesses of approximately 10, 20, and 50 nm. All reported thicknesses were measured on flat glass by ellipsometry for the Si layers or by stylus profilometry for the NiO_x layers. Sputter deposition was carried out at a substrate temperature of 60 °C with a working pressure of 1.70 μbar using a 4-in ceramic NiO target in a chamber with ~3–5×10^{-7} mbar base pressure. Oxygen was supplied to the chamber as a mixture of 5% O_2 in Ar at flow rates of $\sim$0–9 standard cubic centimeters per minute (sccm) (corresponding to 0–4.5% O_2; we will use flow rate values herein) with the balance required to maintain the working pressure made up by pure Ar and a constant total flow rate. After NiO_x deposition, cells were finished by sputtering tin-doped indium oxide (ITO), followed by silver full area on the back and through shadow masks on the front, to define three $\sim$ 1 cm $\times$ 1 cm cells per quarter wafer. Cells were then annealed in air for 20 min at 210 °C. Current–voltage characteristics (JV) were collected on finished cells using a Wacom Electric Co. Super Solar Simulator with AM 1.5G illumination and Keithley sourcemeters.

III. RESULTS AND DISCUSSION

A. Simulated Sensitivity of Materials Parameters

Using AFORS-HET, we simulate the solar cell performance for the various scenarios depicted in Fig. 1. Unless a given parameter is being varied, the default values of the p-layer are assigned to those of "Standard (p) NiO_x" in Table I—namely t = 10 nm, $N_A = 5\times10^{15}$ cm^{-3}, and $\mu_h = 0.151$ $cm^2V^{-1}s^{-1}$—with the exception of E_{VB}, which is assigned to the optimal value of 5.5 eV as discussed subsequently. Note that the low doping and low mobility are intended to be representative of a weakly p-type and poorly ordered material, as is expected to be the case for the envisioned new materials.

1) Single-Parameter Sensitivity Analysis: To first illustrate our single-parameter sensitivity analyses, we simulate the influence of thickness on solar cell properties, and plot results in Fig. 2(a) and (b). Simulated JV curves are shown in panel (a) and tracked FF and efficiencies (η) are shown in panel (b), with blue shading indicating the ranges of highest cell efficiency. We find that the thinnest p-layers ($\sim$10 nm or less) lead to highest performances, with maximum efficiencies and FF of $\sim$23.8% and $\sim$84.8%, respectively. Above 10 nm, an S-shaped JV curve is observed, which leads to a significant drop in efficiency and FF. V_{OC} remains constant, but J_{SC} begins to decrease for thicknesses greater than $\sim$90 nm until efficiency is effectively zero at 200 nm. We note that this simulation does not include tunneling effects. The thickness is an extrinsic parameter and can be varied during growth for any given material; we will focus more on intrinsic materials parameters herein to align with our materials discovery approach.

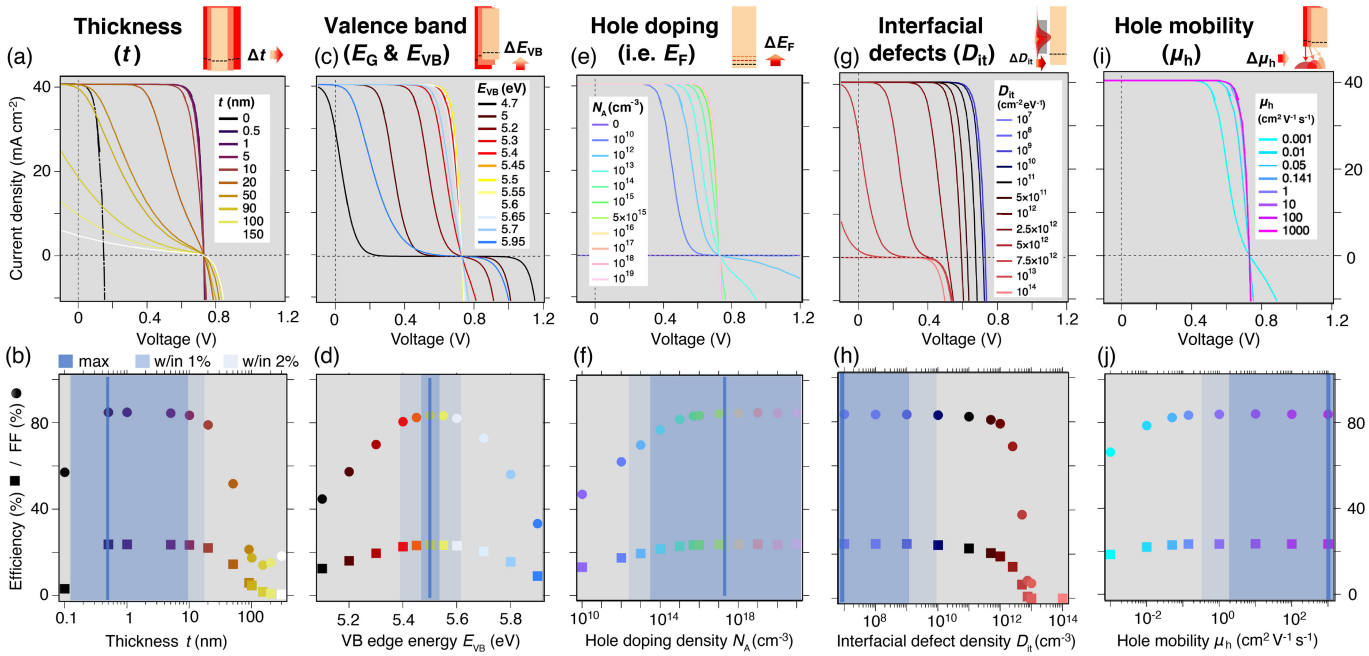

Fig. 2. (Top row) Simulated JV curves and (bottom row) plotted solar cell characteristics for the variations of five material parameters depicted in Fig. 1: (a) and (b) thickness, (c) and (d) valence band edge energy, (e) and (f) hole doping, (g) and (h) interfacial defect density, and (i) and (j) hole mobility. Blue shaded regions in the bottom row indicate regions where the FF is within 1% and 2% of the maximum simulated value.

Second, we assess the influence of the valence band edge energy E_{VB} on simulated solar cell properties, and plot results in Fig. 2(c) and (d). By varying E_{VB} with other parameters constant, we observe an optimal solar cell performance at E_{VB} of 5.5 eV, which correlates to an electron affinity of 2.3 eV with a gap of 3.2 eV. For a hole doping density of 5×10^{15} cm^{-3}, highest efficiency and FF values are ~24.8% and ~84.4%, respectively. FF and efficiency remain at 2% of the optimal value for VB edge offsets (referring here to the offset from the optimum, not the offset with $E_{\mathrm{VB,c\text{-}Si}}$ or $E_{\mathrm{VB,a\text{-}Si:H}}$) of ±0.1 eV, and then drop relatively symmetrically on either side. At the optimal E_{VB} alignment, the JV curves appear ideal, while an S-shape onset occurs at misaligned E_{VB} values. These curves all appear to have the same J_{SC} and V_{OC}, although in the misaligned cases, the JV curve flattens out at lower voltages. Importantly, the optimal E_{VB} does *not* occur at $E_{\mathrm{VB,c\text{-}Si}}$ (5.16 eV), as we had initially hypothesized since the (i) a-Si:H layer is so thin. Rather, it is closer to $E_{\mathrm{VB,a\text{-}Si:H}}$ (5.62 eV), but in fact at a slightly lower energy of 5.5 eV (closer to vacuum). This may indicate that the desired p-layer E_{VB} alignment for the optimal performance is to the *quasi-Fermi energy* of holes ($E_{\mathrm{F,p}}$) at the (i) a-Si:H / p-layer interface under the illumination and standard operating conditions, rather than simply to $E_{\mathrm{VB,a\text{-}Si:H}}$.

Next, Fig. 2(e) and (f) demonstrate that solar cell performance increases with higher hole doping in the p-layer, as expected, but only up to a certain threshold doping. For an E_{VB} of 5.5 eV, so long as doping is greater than approximately 10^{16} cm^{-3}, FF and η only negligibly improve. Below 10^{15} cm^{-3}, FF decreases according to simulations, and we would expect V_{OC} to decrease in an experimental device where defects are included as in Fig. 2(g) (see next section). This suggests that in the SHJ device configuration explored in this article, hole doping does not have to be as high as initially expected, so long as E_{VB} is within 5.5 ± 0.1 eV, and passivation is sufficient.

Using the defect-layer approach outlined in Section II, we fix other parameters and vary interfacial defect density D_{it}. We find in Fig. 2(g) and (h) that solar cell performance remains unchanged to D_{it} values up to ~10^8 $\mathrm{cm}^{-2}\mathrm{eV}^{-1}$, after which the V_{OC} begins to drop with increased D_{it}. At about 10^{11} $\mathrm{cm}^{-2}\mathrm{eV}^{-1}$, efficiency has decreased by over 15%. At D_{it} values greater than ~2.5×10^{12} $\mathrm{cm}^{-2}\mathrm{eV}^{-1}$, FF starts to drop significantly, and efficiencies of cells with $D_{\mathrm{it}} > 10^{13}$ $\mathrm{cm}^{-2}\mathrm{eV}^{-1}$ are effectively zero. These findings corroborate literature reports for NiO_x cells, where increasing D_{it} above ~2×10^{10} $\mathrm{cm}^{-2}\mathrm{eV}^{-1}$ led to a steep decline in efficiency [21], although only one set of conditions was assessed. We acknowledge that it is actually a function of both the capture cross section and D_{it} that influences recombination rates, and thus, V_{OC} [40], although we refer only to D_{it} herein for simplicity. As with all these parameters discussed so far, only D_{it} is varied here, omitting important cross interactions. To get the full picture, it is important to assess the influence of each parameter on one another and this will be done in the next subsection.

Panels (i) and (j) demonstrate that hole mobility (μ_{h}) is less important than the other parameters discussed so far. In this case, we hold the ratio between hole and electron mobility constant at 1:3, and vary hole mobility by six orders of magnitude. Similarly to N_{A}, increasing μ_{h} does indeed increase the performance, although less significantly than the other parameters and only up to a threshold. Anything greater than approximately 0.1 $\mathrm{cm}^2\mathrm{V}^{-1}\mathrm{s}^{-1}$ yields only negligible improvements. This finding is favorable, since very few optically transparent materials with highly mobile holes exist in practice. However, we acknowledge

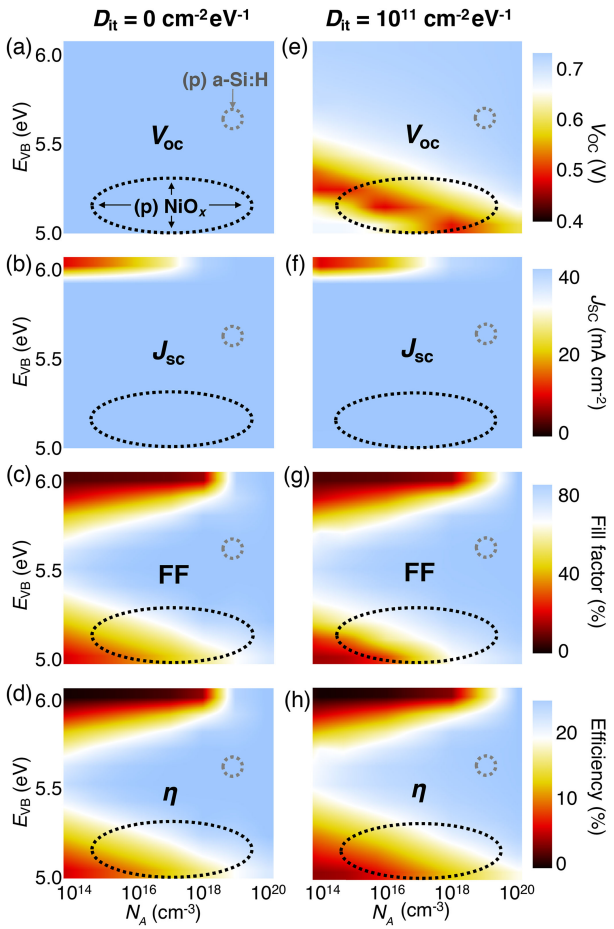

Fig. 3. Heat maps depicting the simultaneous influence of doping (N_A) and valence band edge energy (E_{VB}) on simulated SHJ solar cell properties. (a) Open-circuit voltage V_{OC}, (b) short-circuit current density J_{SC}, (c) fill factor (FF), and (d) efficiency η for a p-layer with no interfacial defect densities. (e)–(h) plot the same heat maps, respectively, but include interfacial defect densities of 10^{11} cm^{-2}eV^{-1}. The dotted ovals indicate approximate experimental ranges of E_{VB} and hole doping density reported in the literature for (p) NiO_x (black) and (p) a-Si:H (gray).

that this relies on the assumption that our choice of VB effective density of state (DOS) N_V (10^{20}cm^{-3}) is reasonable. We also find that independently varying the conduction band energy E_{CB} in this configuration has a negligible effect on the solar cell performance. Additionally changing E_G has a negligible impact in this model until E_G is less than that of c-Si ($E_{G,c\text{-}Si}$ = 1.124 eV), although we note that band gaps in the visible range (less than ∼3.1 eV) can induce parasitic absorption in real devices, which is not accounted for in this simulation. Thus, these findings are not reported in Fig. 2.

2) Multiparameter Sensitivity Analysis: In Fig. 3, we plot heat maps depicting multiparameter variation of N_A and E_{VB} in the p-layer, for D_{it} values of 0 and 10^{11} cm^{-2}eV^{-1}, on the solar cell's V_{OC}, J_{SC}, FF, and efficiency (η). These simulations assume a p-layer thickness of 10 nm, and other "variable p-layer" parameters from Table I. The blue regions in panels (d) and (h) correspond to highest efficiencies, with white indicating a drop to below 20% efficiency. For cells with no D_{it} in (a)–(d), regardless of doping, we observe the highest solar cell performance at E_{VB} values of 5.5 eV, corroborating the optimal alignment from Fig. 2. Fig. 3(c) shows that the drops in efficiency stem nearly entirely from reductions in FF, where JV curves are S-shaped. The panel (b) shows J_{SC} remains relatively constant, except at E_{VB} values of 6 eV or greater and N_A below 10^{18} cm^{-3}, while (a) shows V_{OC} remains constant in this simulation space. Notably, we observe a window of high performance that is narrow at low N_A and widens at higher N_A. This suggests that p-layers with high hole doping are more tolerant to misalignments in VB edge position, while those with low N_A only perform well if their E_{VB} is nearly exactly 5.5 eV. Both positive and negative misalignments lead to reduced performance, although too-high E_{VB} values drop off even steeper than too-low values due to an additional drop in J_{SC}, and we will investigate the physical reasons for these trends subsequently.

Fig. 3(e)–(h) depicts simulated cells with all the same conditions except for an increased D_{it} of 10^{11} cm^{-2}eV^{-1}, which demonstrates the interplay of three materials parameters from Fig. 1. The biggest distinction is shown in Fig. 3(e): the reduction in V_{OC} for lower values of E_{VB}, likely trending with E_F. This influences efficiency at lower values of E_{VB}. We observe that at a given hole doping, the window of high efficiency reduces somewhat at elevated D_{it}, indicated by the shrinking of the blue region in (h). However, so long as optimal alignment and high doping are retained, high performance is still achievable despite interfacial defects, which is promising for practical applications. Additionally, optimal efficiency is not constant at 5.5 eV as in (d), but rather it is shifted somewhat toward higher E_{VB} as N_A increases; at hole dopings of 10^{20} cm^{-3}, efficiency is highest at E_{VB} values of 5.8–5.9 eV (24.86%) rather than 5.5 eV (24.78%), although differences are quite low. This is due to the tradeoff between the increase of V_{OC} and the decrease of FF with E_{VB}, as depicted in (e) and (g). We note that in the AFORS-HET simulations, V_{OC} is not affected in the absence of defects (a) since no current is extracted; however, since defects are virtually unavoidable in real devices, V_{OC} is expected to be impacted even with low defect densities (e).

In all graphs of Fig. 3, the black dotted ovals indicate the likely experimental range of E_{VB} and N_A in NiO_x, according to reported values in the literature [41]–[43]. Without including detrimental D_{it}, it appears that standard (p) NiO_x with N_A of 5 × 10^{16} cm^{-3} and E_{VB} at 5.0 eV is likely *not* an ideal candidate as a hole-selective contact, since FF and η drop to 27.6% and 8.1%. This only gets worse with high D_{it}, as V_{OC} and FF drop significantly to ∼24% and 644 mV, which lead to efficiencies of ∼6.3%. However, significant engineering advances in electronic properties to lower the VB edge energy farther from vacuum (increase E_{VB}), while maintaining high doping and low D_{it}, could push the performance higher into the blue region. This compares with (p) a-Si:H (gray dotted circles) doped to approximately 10^{19} cm^{-3} [44] with a combined doping and alignment leading to high electronic performance and efficiencies of 25.4%, regardless of D_{it}. Since (p) a-Si:H has ideal N_A and E_{VB}, these contacts have a higher D_{it} tolerance than NiO_x.

3) Band Alignments to Understand Performance Trends, and Discussion of Quasi-Fermi Levels: To illustrate how and why the materials properties discussed previously influence the solar cell performance, we plot simulated band alignment diagrams at various conditions in Fig. 4. In panel (g), we use the FF heatmap

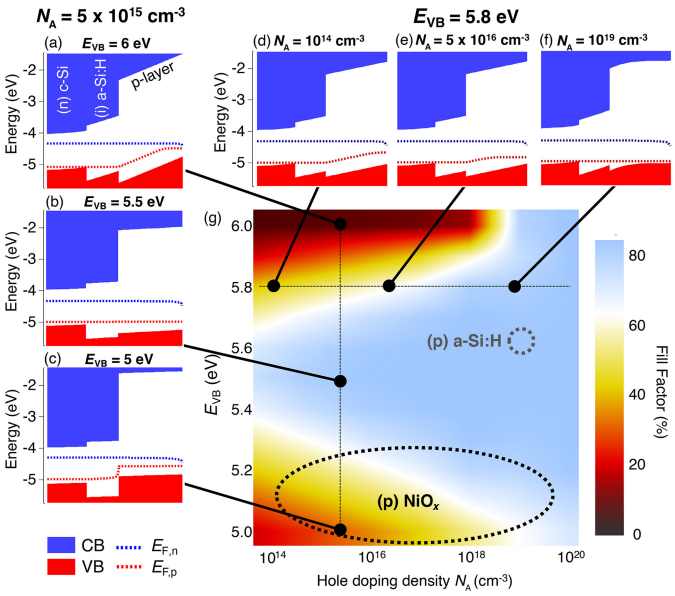

Fig. 4. Band diagrams at maximum power point (MPP) for six different p-layer combinations of VB edge energy (E_{VB}) and hole doping density (N_A). (a)–(c) The three diagrams on the left are at constant N_A and varied E_{VB}, while (d)–(f) the three upper diagrams are at constant E_{VB} and varied N_A. As described in the legend (lower left corner), blue shadings are the conduction band states in the device (CB), dotted blue lines are the electron QFLs ($E_{F,n}$), red shadings are the valence band states in the device (VB), and dotted red lines are the hole QFLs ($E_{F,p}$). Black circles indicate the location of each condition studied on (g), the FF heat map from Fig. 3(c). For reference, the approximate range of E_{VB} and N_A reported experimentally are plotted in (g) for p-type NiO_x and p-type a-Si:H with dotted ovals.

from Fig. 3(c) to guide our location in parameter space, with the vertical thin dotted line indicating constant hole doping and the horizontal thin dotted line indicating constant VB edge energy. Filled black circles indicate the specific conditions investigated. For each circle, band diagrams are plotted under illumination at maximum power point (MPP), where blue shadings are the conduction band states in the device (CB), dotted blue lines are the electron quasi-Fermi levels (QFLs) ($E_{F,n}$), red shadings are the valence band states in the device (VB), and dotted red lines are the hole QFLs ($E_{F,p}$). The (n) c-Si layer is the left-most layer, the (i) a-Si:H is the center layer, and the variable p-layer is the right-most layer, as shown in (a).

First, we observe changes in band alignments at a constant hole doping of 5×10^{15} cm^{-3} in Fig. 4(a)–(c). At the well-aligned E_{VB} value of 5.5 eV depicted in (b), the position of $E_{F,p}$ is preserved throughout the p-layer at the same energy level as in the c-Si layer. This is the signature of a high-performing hole contact [47]. At misaligned E_{VB} values of 6.0 eV (a), however, the p-layer is depleted due to the band offset, and, thus, band edges bend upwards sharply. Under illumination, $E_{F,p}$ also bends upwards due to the resistivity of this depleted layer, and nearly meets the $E_{F,n}$ over the thickness of the p-layer. This results in a loss of QFL splitting—the difference between the electron QFL ($E_{F,n}$) and hole QFL ($E_{F,p}$)—inside the contact itself. Thus, we would expect thinner layers or layers of higher mobility to perform better at this condition. Finally, at misaligned E_{VB} values of 5.0 eV depicted in (c), QFL splitting is lost immediately at the onset of the p-layer due to the sharp positive VB edge offset. This is the case that correlates approximately with standard NiO_x. Here, $E_{F,p}$ in the p-layer is too low (around 4.5 eV), which leads to a hole depletion along the (i) a-Si:H layer that causes the drop in $E_{F,p}$ at the (i) a-Si:H / p-layer interface upon charge extraction.

Second, in Fig. 4(d)–(f), we observe changes in band alignments at a constant E_{VB} of 5.8 eV, where a negative band offset leads to similar upward $E_{F,p}$ bending. At low hole doping values of 10^{14} cm^{-3} in (d), the situation is similar to that in (a), with $E_{F,p}$ decreasing through the contact due to the resistance in the depleted p-layer. As doping increases in (e), a flat $E_{F,p}$ can be maintained in part of the contact thickness due to the larger hole reservoir in this higher doped layer, enabling a higher conductivity to hole extraction in this illuminated device scenario. This allows for a larger QFL splitting to be maintained, which mitigates the S-shape and improves the FF. At N_A densities of 10^{19} cm^{-3} (f), high doping leads to a narrow depleted thickness in the p-layer, which ensures a high conductivity of the p-layer throughout its thickness (including within the depletion zone). Importantly, in these iso-E_{VB} simulations, the work function E_F increases with doping, also influencing the band bending. This is similar to the formation of an Ohmic contact between a highly doped semiconductor and a metal. In such a situation, the $E_{F,p}$ does not bend upwards at all and the performance is optimal.

This assessment reveals the importance of the p-layer's Fermi level in the determination of the performance of the entire SHJ cell, and highlights that high doping is key to enable nonideally aligned materials to still perform well as hole-selective contacts. This high doping is also key to ensure a good contact with the eventual transparent electrode, which makes it a stringent feature for any novel p-type material [48]. As a concluding note for this simulation section, we emphasize that the results shown here are only guidelines for idealized systems, and that effects stemming from the influence of the transparent electrode or from Fermi level pinning were not accounted for. Additionally, only 1-D effects were simulated, and the rudimentary optical model used in AFORS-HET may be oversimplifying optical effects. Accurate reproduction of these phenomena lie beyond the scope of this simulation software, yet is a crucial part of real-world solar cells.

B. Case Study: Sputtered p-Type NiO_x as a Hole-Selective Contact

To illustrate the influence of various p-layer parameters from Fig. 1 on solar cell properties, we fabricate SHJ devices using sputtered p-type NiO_x as a test-case variable p-layer, as depicted in Fig. 5(a). A representative crystal structure of NiO_x is shown in Fig. 5(b) (in this case, with $x = 1.2$). It is a derivative structure of rocksalt NiO, where Ni vacancies lead to off-stoichiometries ($x > 1$), structural distortions, and p-type conductivity [49]. NiO_x is selected as a test material because its valence band edge energy, E_{VB,NiO_x}, is approximately aligned with that of c-Si, $E_{VB,c\text{-}Si}$, as depicted in Fig. 5(c)—this was our initial hypothesis of what leads to high performance. Additionally, we expect some tunability of hole doping and E_{VB,NiO_x} with the O/Ni ratio, x,

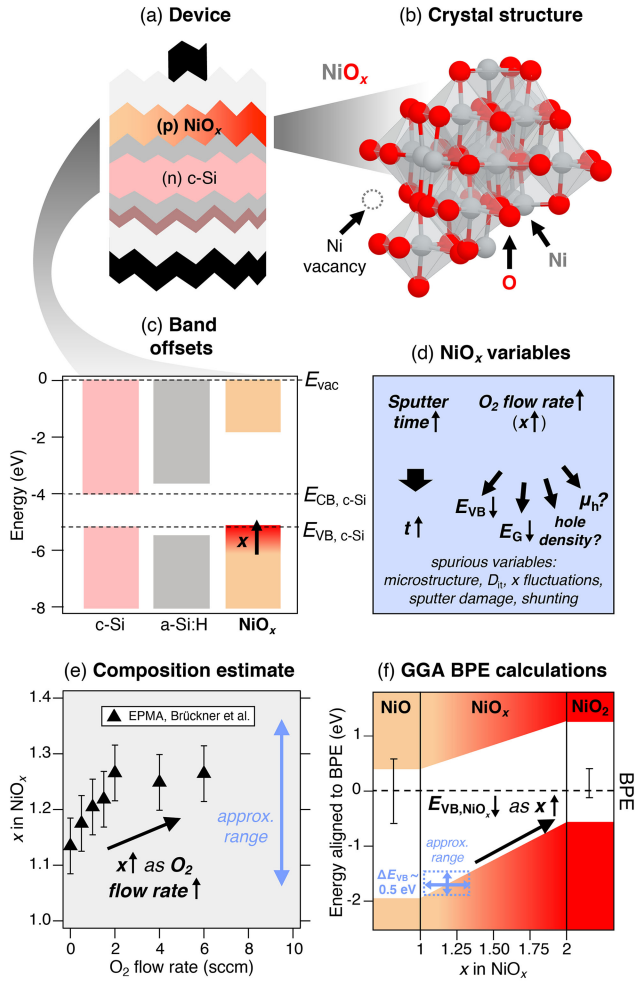

Fig. 5. (a) Device schematic with NiO_x as the p-type hole-selective contact, with a red gradient indicating variable properties in this study. (b) Crystal structure of a representative NiO_x compound (Ni_5O_6, mp-754806), where Ni vacancies lead to p-type conductivity and local distortions [45]. (c) Band offset schematic of the three simulated layers, comparing NiO_x to n-Si and a-Si:H. Dotted lines correspond to the band edges of c-Si and the vacuum energy E_{vac}. The red gradient and "x" label illustrates that the VB edge energy moves closer to E_{vac} as x increases. (d) Extrinsic parameters targeted in our experiments, and their influence on intrinsic parameters. (e) Approximate x values for the given O_2 flow rate, with literature values from Brückner *et al.* [46]. (f) Band positions of rocksalt NiO and layered NiO_2 calculated using a GGA functional and aligned to BPE values. Note that this is a *qualitative* alignment, and the y-axis energies are not equivalent to the *quantitative* alignment energies in (c). For NiO_x, compounds between these two end points, we plot a linear relation assuming commensurate structures and no bowing. Thus, we would expect the VB edge to shift toward vacuum as x increases.

as explained subsequently. Because of inherent limitations of sputter synthesis and available characterization tools, we neither can directly vary all of the six parameters in Fig. 1(b), nor can we measure each with certainty; therefore, we limit our extrinsic variables to oxygen (O_2) flow rate and thickness t. These variables should induce changes in intrinsic variables as depicted in Fig. 5(d), although we note that varying the O_2 flow rate influences multiple material parameters. Namely, we expect E_{VB,NiO_x} to shift toward vacuum with increased x and the band gap E_G to decrease, as elaborated subsequently. Additionally, it has been reported by numerous studies that increasing O_2 flow during sputter growth reduces resistivity (i.e., increases conductivity) in p-type NiO_x [43], [50]–[53]. Some reports indicate an increase in hole doping and decrease in mobility [52], [53], but trends and magnitudes are inconsistent [43], [51]. Interfacial defect density D_{it} is left as a modeled parameter.

1) NiO_x Parameter Space: The relations between O_2 flow during synthesis, x in NiO_x, and resulting hole doping and E_{VB,NiO_x} are not reported together in the literature, to our knowledge. Although widely accepted that $x > 1$, the value of x in NiO_x is rarely reported, and even more rarely as a function of synthesis conditions. Brückner *et al.* report electron probe microanalysis (EPMA) quantification of RF sputtered NiO_x at varying O_2 gas flows, with synthesis conditions similar to ours but not identical, demonstrating an increase of x with O_2 flow as shown in Fig. 5(e) with triangular markers (error bars from EPMA measurement) [46]. We roughly estimate that varying O_2 flow in our study from 0 to 9 sccm likely yields an increase of x, likely somewhere between 1 and 1.4 (blue arrow). We emphasize that parameters such as chamber design and deposition conditions limit the *quantitative* transferability of these literature values, and that x should be confirmed for our samples by EPMA or another standard-free quantification method. However, what is important here is the *qualitative* demonstration that the increase of O_2 results in the increase of x, and this qualitative trend has been corroborated by other studies using metallic Ni targets [41], [42].

In order to assess the role of x on E_{VB,NiO_x} and E_{G,NiO_x}, we obtain uniform band structure calculations from the Materials Project database of end-points NiO and NiO_2 ($x = 1$ and $x = 2$, respectively), and calculate their corresponding BPE values. BPE is a computationally inexpensive metric to qualitatively compare band alignments [16], [38]. In Fig. 5(f), NiO (left) and NiO_2 (right) are aligned to their respective BPE values, denoted by the dashed line, and BPE is estimated for in-between compositions of NiO_x assuming commensurate structures and Vegard's law with no band bowing. Error bars are calculated using the procedure outlined in Woods-Robinson *et al.* [16]. This suggests that increasing x from 1 to 2 results in a significantly increased E_{VB,NiO_x} (by ~1.25 eV), a slightly increased E_{CB,NiO_x} (a value typically held constant in the literature) [30], and slightly decreased E_{G,NiO_x} as expected from experimental studies [54]. For NiO_2, we plot the experimental layered structure (mp-35925); a structural relationship has been shown in the literature between layered structures and disordered rocksalt structures [55] that supports this choice of end-point compound, although this trend applies for other NiO_2 polymorphs too (e.g., mp-25428). This relation is merely qualitative; NiO_x is a notoriously tricky system to model computationally due to its complex defect chemistry and magnetic ordering [49], and precise alignment calculations are beyond the scope of this study. Furthermore, our NiO_x films are likely amorphous [56], and band edges of amorphous semiconductors are not as sharply defined as those of crystalline materials. However, the key point is that we expect x to increase and E_{VB,NiO_x} to shift to lower energy values (closer to vacuum) upon increasing O_2 flow in the sputter gas. This correlation is supported by Keraudy *et al.*'s report of an increase of E_{VB,NiO_x} as x is increased from 1.01 to 1.14 [54], yet this study uses a metallic

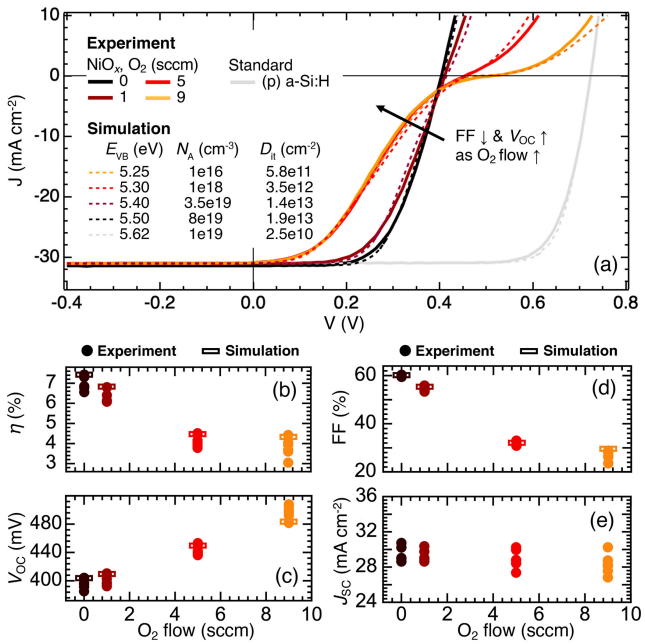

Fig. 6. (a) JV curves for NiO_x-contacted SHJ solar cells (solid lines), with oxygen flow rates in the NiO_x layer of 0, 1, 5, and 9 sccm, and for a standard cell with a (p) a-Si:H contact. Fits for the simulations used in this study are shown with dashed lines, with simulated parameters reported in the legend. Statistical analysis of these cells for solar cell performance parameters: (b) efficiency (η), (c) V_{OC}, (d) fill factor (FF), and (e) J_{SC}.

TABLE II
BEST SOLAR CELL RESULTS FOR SHJ CELLS WITH NiO_x HOLE-SELECTIVE CONTACTS AT VARIOUS OXYGEN GROWTH CONDITIONS, COMPARED WITH A STANDARD CELL FABRICATED WITH A (P) A-SI:H CONTACT

Flow rate (sccm)	O_2 (%)	η (%)	FF (%)	V_{OC} (mV)	J_{SC} (mA cm^{-2})	R_S (Ω cm^2)
0	0	7.432	59.94	403.6	30.73	2.72
1	0.5	6.807	54.61	410.6	30.36	3.88
5	2.5	4.511	32.91	453.3	30.24	9.53
9	4.5	4.424	28.81	507.9	30.24	11.54
(p) a-Si:H		16.72	78.45	724.4	29.42	2.523

Ni target and impulse magnetron sputtering discharge rather than RF sputtering, so O_2 flow cannot be directly compared.

2) NiO_x JV Results and Simulation Fits: Fig. 6(a)–(e) reports the JV and performance results of a set of SHJ solar cells with NiO_x hole-selective contacts and varied O_2 flow rate (in sccm) during the NiO_x growth. In the panel (a), experimental JV curves are reported with solid lines, and the light gray curve corresponds to a standard cell with a (p) a-Si:H hole contact. All of the NiO_x cells have relatively poor V_{OC} values, ranging between ~400 and 500 mV as reported in Table II for the four highest efficiency cells at each condition, and V_{OC} increases slightly with O_2 flow. The JV curves all have S-shapes, but increasing O_2 flow results in lower FF, lower efficiencies, and more exaggerated S-shapes, with a flattening out of the JV curve around the V_{OC}. J_{SC} values are scattered due to the rudimentary metallization made by shadow masking without influence from O_2 flow. By varying and optimizing O_2 flow and NiO_x thicknesses, we achieve efficiencies over 7% (O-poor growth conditions) and a maximum V_{OC} of just over 500 mV (O-rich growth conditions). This is low compared to standard cells with a (p) a-Si:H hole-selective contact, with V_{OC} and efficiency of 724.4 mV and 16.72%, respectively, as reported in Table II. However, the trends revealed here and their connection to simulated material parameters still yield important considerations for contact design.

To explore the link between our modeling and experiments, we can fit the NiO_x JV results from Fig. 6 to our AFORS-HET simulations by varying hole doping N_A, E_{VB,NiO_x}, and interfacial defect density D_{it}. We estimate that E_{VB,NiO_x} decreases by up to ~0.5 eV with increased O_2 flow (E_{VB,NiO_x} moves closer to vacuum), as backed out from Fig. 5(e) and (f) [46], [54]. Hole doping has been reported to widely vary in NiO_x; for low hole doping densities, a VB edge offset of just a few hundred meV should have a significant impact according to our model, but studies have reported hole doping densities up to $\sim 8 \times 10^{19}$ cm^{-3}, which would give more leniency to E_{VB,NiO_x} [52]. An example of such fits is plotted with dashed lines in Fig. 6(a) for a set of representative JV curves corresponding to O_2 flows of 0, 1, 5, and 9 sccm, with a fixed thickness of 20–25 nm, hole mobility of 0.1 cm^{2}V^{-1}s^{-1}, and fit values reported in the figure legend. Fits are performed as well for a baseline (p) a-Si:H sample, with $E_{VB,a\text{-}Si:H}$ constrained at 5.62 eV, $N_A = 10^{19}$ cm^{-3}, and $\mu_h = 5$ cm^{2}V^{-1}s^{-1}. A small series resistance of 0.8 Ω cm^2 is added for (p) a-Si:H to improve the fit, and likewise series resistances are added for the NiO_x cell fits (fitting values are determined by scaling the (p) a-Si:H value according to experimental R_S values from Table II). The current density is normalized in the simulations to match experimental JV curves, since shadow masking has reduced the J_{SC}. We find the simulations to align with experimental results, which yield similar V_{OC}, FF, and efficiency values as reported with rectangular markers in Fig. 6(b)–(e), as well as closely aligned JV profiles.

Most importantly, this analysis suggests that as x increases in NiO_x, E_{VB,NiO_x} decreases away from the optimum value, D_{it} decreases, and doping increases. In other words, as O_2 flow increases, the material is likely less resistive (depending on μ_h), the valence band edge is increasingly misaligned, and the contact is likely better passivated (although still not very passivated). This explains the tradeoff between V_{OC} and FF in the experimental cells, and the increased S-shape and flattening of JV around V_{OC} as O_2 flow increases. Although useful, we emphasize the reductive nature of fitting; multiple fit values can match experimental data. Therefore, we caution quantitative interpretation of these results. Namely, simulated E_{VB,NiO_x} is somewhat higher than expected from the literature, and the simulated hole doping density for the 0 sccm fit is at the high end for experimental values [52]. Additionally, fit values are only estimates since the simulations ignore intrinsic defects, contact resistances, and other effects. For follow-up work, a measurement of one of the values of E_{VB} or doping density is important to appropriately constrain the model. We previously measured cells with NiO_x thicknesses varying from 10 to 100 nm grown at 0 and 1 sccm [56]. These results demonstrate that performance, namely, FF, drops very slightly for thicker NiO_x, also corroborating simulations. Thus, by combining theoretical modeling and real cell measurements, we have demonstrated a

link between simulated and experimental performance that can inform searches for a hole-selective contact that is better than NiO_x.

3) Role of Interfacial Defects and Nonidealities: A key takeaway here is that D_{it} is very high in all NiO_x cells: nonidealities, likely at the interface, are apparently reducing the performance of these cells. Even the case with the lowest D_{it} is still over an order of magnitude worse than the performance modeled in the (p) a-Si:H cell. Nayak *et al.* have recently achieved higher performing cells with a NiO_x p-layer [22], which is probably due to better passivation and lower D_{it}, but we note that this device architecture does *not* use an intrinsic a-Si:H layer, so our simulation is not directly transferable here. This corroborates our simulations from Fig. 2(a) and (b). If D_{it} can be reduced while maintaining the same material parameters, higher efficiencies could be achieved as shown in Fig. 3, but only within a very narrow window of parameter space.

The parameter "D_{it}" is a cumulative proxy for a wide array of nonidealities that could be occurring in this system as a result of thermodynamic limits, kinetic effects such as sputter damage, and other growth conditions. Defects represented by D_{it} could induce surface pinning, and could be caused by interfacial layers, phase segregation, and other defects not modeled here including point defects, band edge tail states, extended defects, etc. One likely mechanism that could lead to nonidealities and high D_{it} is the chemical instability of the Si/NiO_x interface and the possible formation of a spurious interfacial layer. To assess whether this may be occurring, we calculate the possible reactions between Si and NiO_x, assuming thermodynamic equilibrium and 0 K using the Materials Project's Interfacial Reaction Calculator [45], [58]. We find the following reaction as likely to occur at the interface:

$$x\ \mathrm{Si} + 2\ \mathrm{NiO}_x \longrightarrow 2x\ \mathrm{Ni} + x\ \mathrm{SiO}_2 \tag{1}$$

with a reaction enthalpy of -196.8 kJ/mol (-1.224 eV/atom). This finding corroborates literature findings, which report a Gibbs free energy change at 1000 K of -51.377 kcal/mol [59]. Additionally, a thin SiO_x is almost certainly forming when the Si wafer is exposed to air. However, change transport in a thin SiO_x layer would likely involve tunnelling through a barrier, and we reiterate that such tunneling is not included in our simulations and is a limitation of our model. Other possible interfacial reactions could result in the formation of ternary spinel or ilmenite Ni_2SiO_4 [60] or metal alloy $NiSi_x$ [61]. This formation may cause a trapping layer, leading to increased D_{it} and other effects. However, as shown recently, it is also possible that SiO_x is forming at the interface without a significant detrimental effect on passivation [62]. In fact, Nayak *et al.* reported that an intentionally introduced SiO_x layer actually improves the solar cell performance in (n) c-Si / (i) SiO_x / (p) NiO_x devices [22]. The implications for an (n) c-Si / (i) a-Si:H / (i) SiO_x/ (p) NiO_x device remain to be explored. Additionally, it remains to be investigated whether spurious phases of the Ni metal or Ni_2O_3 are present, the role of point defects and extended defects in NiO_x, whether hydrogenated NiO_x:H is formed, and whether such hydrogenation or phase segregation could enhance the passivation and minimize D_{it}.

C. Prospective: Exploring New Hole-Selective Contacts in SHJ Solar Cells

The insights gained from our simulations and the implementation of NiO_x as a test material can guide the selection of new materials as hole-selective contacts in SHJ solar cells with (i) a-Si:H passivation layers. In particular, we hypothesize that the alignment of the p-layer's E_{VB} to $E_{VB,a\text{-}Si:H}$ is more important than alignment to $E_{VB,c\text{-}Si}$. Assuming low D_{it}, the offset between E_{VB} and $E_{VB,a\text{-}Si:H}$ should be within approximately ± 0.3 eV for high doping densities ($N_A > 10^{18}$ cm^{-3}), with a narrower window when doping is decreased (within ± 0.1 eV for 10^{16} cm^{-3}). This combination of misaligned E_{VB} and insufficient doping (as well as defects, thickness, mobility, etc.) might be a reason for the common observation of S-shaped JV curves when integrating novel materials as contacts for SHJ devices. It also is likely why the typical (p) a-Si:H contact performs so well—it is highly dopable, it has a clean interface with (i) a-Si:H, and its VB edge is perfectly aligned to that of (i) a-Si:H since it is the same material.

Using the criteria outlined in this study, we can define a materials discovery pipeline using a "screening funnel" to search for new hole-selective contacts in SHJ solar cells, depicted in Fig. 7(a). A screening funnel is a series of criteria that a material must pass in order to be considered for a certain application [63]. Here, we consider an *ab initio* computational screening procedure using DFT that can be used by other researchers while searching for new hole-selective contacts. First, for this application it is useful (although not mandatory) to start with a search space of materials that have been experimentally synthesized. Second, to avoid parasitic absorption, only semitransparent materials with band gaps greater than approximately 2 eV must be considered (note that this value depends on the DFT functional used; calculations using the PBE GGA functional and associated calculation parameters used in the Materials Project database systematically underestimate the band gap by 50–100%) [64]. We note that the optical absorption coefficient could also be used in this step, but band gap is computationally "cheaper" to calculate, therefore, most high-throughput studies use a band gap cutoff as a proxy for the absorption edge. Additionally, we note that this band gap criterion would exclude (p) a-Si:H, as it is not sufficiently transparent. Third, the material should ideally be p-type dopable, although we acknowledge notable exceptions such as MoO_x: an alternate contact design approach could use a tunnel or defect recombination junction with an n-type material. Since p-type doping is trickier to assess computationally [65], only the experimentally confirmed p-type materials are considered subsequently, but one could use defect calculations to calculate dopability in a screening [66]. Fourth, as discussed previously, the VB edge energy should be aligned to within ± 0.3 eV of that of a-Si:H, although the alignment does not have to be so sharp if doping is high enough. And fifth, as discussed in the previous section, a chemically stable interface with Si is preferable (although not required) to prevent spurious interfacial defects. Other important criteria, such as bond strength and resistance to sputter damage, could be added sequentially after the fifth step. Additionally, the hole-selective

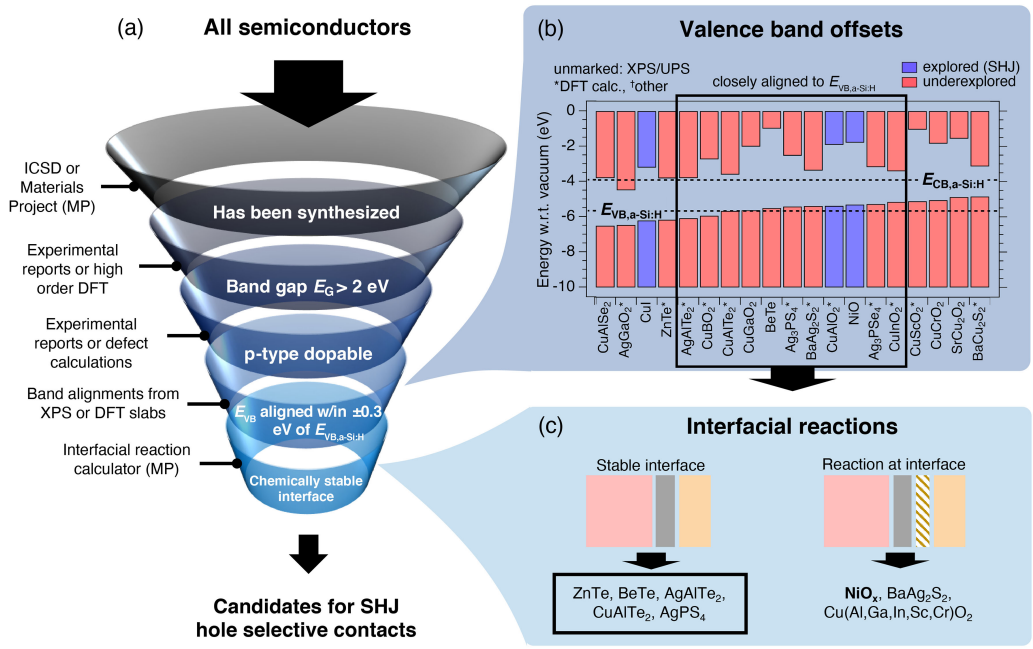

Fig. 7. (a) "Screening funnel" to search for new candidates as hole-selective contacts in SHJ solar cells. (b) Band alignment of possible hole-selective contact materials for SHJ solar cells (funnel rung #4), with references for each material's alignment reported by Woods-Robinson *et al.* [16], [57]. (c) Interfacial reaction calculations of contact materials that resulted from (b), where the extra brown-striped layer indicates an unwanted reaction at the interface (funnel rung #5).

material must make good Ohmic contact to a metal (e.g., Ag) in order to transport charge out of the cell, which may not be trivial (we have assumed an ideal Ohmic contact throughout). This is another positive aspect of having high doping in the p-layer, and the choice of metal will depend on the band alignment.

In Fig. 7(b) and (c), we apply this funnel to a small test set to illustrate its function and to suggest a few candidates for future exploration. Fig. 7(b) compares the band offsets for a series of wide band gap p-type materials from the experimental literature (that satisfy the first three steps of the funnel), and a box is drawn around the materials with potential promise for SHJ solar cells according to their E_{VB}. These materials and their offsets are selected from experimentally realized p-type transparent conductors [16] and from a set of p-type wide band gap chalcogenides [57]. We indicate which of these have been explored in SHJ solar cells (purple), as discussed in the introduction, but many listed materials remain underexplored for device applications (red). Band offsets are from the literature and are derived from both XPS studies and DFT calculations (the latter notated with an asterisk). Perhaps, more importantly, understanding of this alignment could lead to a new screening descriptor to inform future computational material discovery studies.

In Fig. 7(c), we use the Materials Project's Interfacial Reaction Calculator to compute reaction energies for the series of materials that emerge from (b) [58]. We find that at thermodynamic equilibrium, a majority of the compounds boxed in (b), including NiO_x, are likely to form a reaction product with Si. In particular, the delafossite materials CuMO$_2$ (M = Al, Ga, In, Sc, and Cr) are predicted to form $\mathrm{SiO_2}$ and other ternary products, while $\mathrm{BaAg_2S_2}$ is predicted to form ternary products $\mathrm{BaAg_8S_5}$ and $\mathrm{Ba_3SiS_5}$. This formation may or may not be detrimental, as discussed previously, although it adds complication to the device stack and is worth considering. In this example, only p-type telluride compounds such as ZnTe and $\mathrm{AgPS_4}$ emerge from the screening funnel. ZnTe is used as a p-type contact in CdTe solar cells [67], and can be alloyed to raise E_{VB} closer to vacuum. We note that this calculator is a simple approximation based on convex hull analysis and does not take kinetics into account. Even though they satisfy the funnel criteria, multinary compounds such as $\mathrm{Ag_3PS_4}$ may introduce new challenges into device applications such as detrimental nonequilibrium phase segregation, and if sputter deposited, increased sputter damage. Notably, this test example is only a small subset of possible wide band gap p-type materials. Many computationally predicted p-type transparent conductors (e.g., ZrOS [18], BP [17], and $\mathrm{La_2SeO_2}$ [68]) await experimental investigation and may prove to have appropriate VB edge alignment, dopability, and stability for use as a hole-selective contact in SHJ applications.

IV. Conclusion

In SHJ solar cells, a wide band gap p-type hole-selective contact ("p-layer") with appropriate alignment, doping, and passivation, should reduce parasitic absorption and improve FF compared to the standard (p) a-Si:H layer. In this study, we first have used simulations to perform a sensitivity analysis of various material parameters for such a p-layer in a simplified device configuration of (n) c-Si / (i) a-Si:H / p-layer. We have observed that the VB edge energy E_{VB}, p-type doping, D_{it}, and thickness are the most important parameters. In particular, we have hypothesized that the VB edge alignment between the p-layer and (i) a-Si:H is more important than the alignment with the (n) c-Si wafer, which is counter to what has been previously assumed and could explain the commonly observed S-shaped JV curves for previous attempts to incorporate novel

p-type layers as contacts in SHJ cells. We have also found that for nonoptimal E_{VB}, increased doping could improve the cell performance, in some cases, to the same level as for the optimal E_{VB}, so long as D_{it} is low enough. Our simulation results are supported by experiments using NiO_x layers with varying oxygen content (x). Namely, we expect that increasing x should increase the VB offset, and show that doing so degrades FF and efficiency as expected from the simulations. We hypothesize that a very high D_{it} is responsible for low V_{OC} values, and reducing detrimental defects is essential for high performance. Based on these findings, we have suggested a set of semi-transparent compounds with p-type doping and sufficient VB alignments that merit exploration as hole-selective layers in SHJ solar cells.

This study elicits broader implications for both theorists and engineers in the exploration and development of p-type contacts for device applications, and materials design in general. Device engineers tend to work with a small set of well-investigated conventional semiconductor materials (e.g., Si, GaN, ZnO, and ITO) [69]; we have discussed strategies for going beyond this paradigm and pairing engineering with new materials discovery. To guide this process, we emphasize the importance of conducting multiparameter analyses to assess how material parameters should be optimized collectively and to determine the ranges of tolerance that enable a good device performance. For example, we have highlighted the tradeoff between high doping and precise band alignment in the SHJ hole-selective contact. While searching for new materials, it is important to consider that a given material does not have fixed properties, but rather allows for a wide range of tunability. Computational screenings, which usually just calculate bulk properties of alloy end members, ignore such tunability and risk excluding materials on the basis of a false negative, since the end members do not have the desired property, even though the alloy reasonably might [45]. Additionally, tailoring screening criteria to a given application could prove useful; at least for SHJ applications, achieving a high hole mobility may be less important than other criteria, which counters a general assumption in searches for new p-type transparent conductors that high mobility is a necessity [18]. Ultimately, we have demonstrated that a mutually beneficial link between optoelectronic device engineering and computational materials design can be formed: practical material requirements necessary for solving a given device challenge can be used to drive the computational materials design approach while also highlighting new materials for experimental investigation.

Author Contributions

Conceptualization: R. Woods-Robinson, A. N. Fioretti, and M. Boccard; Methodology: R. Woods-Robinson and A. N. Fioretti; Investigation: R. Woods-Robinson, A. N. Fioretti, and M. Boccard; Writing: R. Woods-Robinson; Funding acquisition: R. Woods-Robinson, A. N. Fioretti, M. Boccard, and C. Ballif; Supervision: A. N. Fioretti, J. Haschkeyz, M. Boccard, K. A. Persson, and C. Ballif.

Acknowledgment

The authors would like to thank P. V. Philippe and S. Dunand for technical assistance, and A. L. Massimiliano, Dr. S. Zhong, Dr. S. Dwaraknath, and Dr. M. K. Horton for fruitful discussion.

References

[1] K. Yoshikawa *et al.*, "Silicon heterojunction solar cell with interdigitated back contacts for a photoconversion efficiency over 26%," *Nat. Energy*, vol. 2, no. 5, p. 17032, 2017.

[2] J. Haschke, O. Dupré, M. Boccard, and C. Ballif, "Silicon heterojunction solar cells: Recent technological development and practical aspects—From lab to industry," *Sol. Energy Mater. Sol. Cells*, vol. 187, pp. 140–153, 2018.

[3] A. Onno, C. Chen, P. Koswatta, M. Boccard, and Z. C. Holman, "Passivation, conductivity, and selectivity in solar cell contacts: Concepts and simulations based on a unified partial-resistances framework," *J. Appl. Phys.*, vol. 126, no. 18, p. 183103, 2019.

[4] J. Bullock, A. Cuevas, T. Allen, and C. Battaglia, "Molybdenum oxide $\mathrm{MoO_x}$: A versatile hole contact for silicon solar cells," *Appl. Phys. Lett.*, vol. 105, no. 23, p. 232109, 2014.

[5] J. Geissbühler *et al.*, "22.5% efficient silicon heterojunction solar cell with molybdenum oxide hole collector," *Appl. Phys. Lett.*, vol. 107, no. 8, p. 081601, 2015.

[6] J. Dréon *et al.*, "23.5%-efficient silicon heterojunction silicon solar cell using molybdenum oxide as hole-selective contact," *Nano Energy*, vol. 70, p. 104495, 2020.

[7] L. Mazzarella, S. Kirner, B. Stannowski, L. Korte, B. Rech, and R. Schlatmann, "p-type microcrystalline silicon oxide emitter for silicon heterojunction solar cells allowing current densities above 40 mA/cm2," *Appl. Phys. Lett.*, vol. 106, no. 2, p. 023902, 2015.

[8] A. N. Fioretti, M. Boccard, R. Monnard, and C. Ballif, "Low-temperature *p*-type microcrystalline silicon as carrier selective contact for silicon heterojunction solar cells," *IEEE J. Photovolt.*, vol. 9, no. 5, pp. 1158–1165, Sep. 2019.

[9] A. E. Delahoy and S. Guo, "Transparent conducting oxides for photovoltaics," in *Handbook of Photovoltaic Science and Engineering.* New York, NY, USA: Wiley, 2011, pp. 716–796.

[10] A. Banerjee and K. Chattopadhyay, "Recent developments in the emerging field of crystalline p-type transparent conducting oxide thin films," *Prog. Cryst. Growth Characterization Mater.*, vol. 50, no. 1–3, pp. 52–105, 2005.

[11] A. N. Fioretti and M. Morales-Masis, "Bridging the p-type transparent conductive materials gap: Synthesis approaches for disperse valence band materials," *J. Photon. Energy*, vol. 10, no. 4, p. 042002, 2020.

[12] A. Walsh and J.-S. Park, "The holey grail of transparent electronics," *Matter*, vol. 3, no. 3, pp. 604–606, 2020.

[13] S. Liu, R. Liu, Y. Chen, S. Ho, J. H. Kim, and F. So, "Nickel oxide hole injection/transport layers for efficient solution-processed organic light-emitting diodes," *Chem. Mater.*, vol. 26, no. 15, pp. 4528–4534, 2014.

[14] S. A. Makhlouf, "Electrical properties of NiO films obtained by high-temperature oxidation of nickel," *Thin Solid Films*, vol. 516, no. 10, pp. 3112–3116, 2008.

[15] H. Wu and L.-S. Wang, "A study of nickel monoxide (NiO), nickel dioxide (ONiO), and $\mathrm{Ni(O_2)}$ complex by anion photoelectron spectroscopy," *J. Chem. Phys.*, vol. 107, no. 1, pp. 16–21, 1997.

[16] R. Woods-Robinson, D. Broberg, A. Faghaninia, A. Jain, S. S. Dwaraknath, and K. A. Persson, "Assessing high-throughput descriptors for prediction of transparent conductors," *Chem. Mater.*, vol. 30, no. 22, pp. 8375–8389, 2018.

[17] J. B. Varley, A. Miglio, V.-A. Ha, M. J. van Setten, G.-M. Rignanese, and G. Hautier, "High-throughput design of non-oxide p-type transparent conducting materials: Data mining, search strategy, and identification of boron phosphide," *Chem. Mater.*, vol. 29, no. 6, pp. 2568–2573, 2017.

[18] G. Hautier, A. Miglio, G. Ceder, G.-M. Rignanese, and X. Gonze, "Identification and design principles of low hole effective mass p-type transparent conducting oxides," *Nat. Commun.*, vol. 4, p. 2292, 2013.

[19] G. Brunin, F. Ricci, V.-A. Ha, G.-M. Rignanese, and G. Hautier, "Transparent conducting materials discovery using high-throughput computing," *npj Comput. Mater.*, vol. 5, no. 1, p. 1, 2019.

[20] T. Arai, S. Iimura, J. Kim, Y. Toda, S. Ueda, and H. Hosono, "Chemical design and example of transparent bipolar semiconductors," *J. Amer. Chem. Soc.*, vol. 139, no. 47, pp. 17 175–17 180, 2017.

[21] F. Menchini *et al.*, "Application of NiO_x thin films as p-type emitter layer in heterojunction solar cells," *Phys. Status Solidi c*, vol. 13, no. 10–12, pp. 1006–1010, 2016.

[22] M. Nayak, S. Mandal, A. Pandey, S. Mudgal, S. Singh, and V. K. Komarala, "Nickel oxide hole-selective heterocontact for silicon solar cells: Role of SiO_x interlayer on device performance," *Sol. RRL*, vol. 3, no. 11, p. 1900261, 2019.

[23] R. Stangl, M. Kriegel, and M. Schmidt, "AFORS-HET, version 2.2, a numerical computer program for simulation of heterojunction solar cells and measurements," in *Proc. IEEE 4th World Conf. Photovolt. Energy Conf.*, vol. 2, 2006, pp. 1350–1353.

[24] R. Varache, C. Leendertz, M. Gueunier-Farret, J. Haschke, D. Muñoz, and L. Korte, "Investigation of selective junctions using a newly developed tunnel current model for solar cell applications," *Sol. Energy Mater. Sol. Cells*, vol. 141, pp. 14–23, 2015.

[25] M. Schmidt *et al.*, "Physical aspects of a-Si: H/c-Si hetero-junction solar cells," *Thin Solid Films*, vol. 515, no. 19, pp. 7475–7480, 2007.

[26] J.-P. Kleider, A. Gudovskikh, and P. Roca i Cabarrocas, "Determination of the conduction band offset between hydrogenated amorphous silicon and crystalline silicon from surface inversion layer conductance measurements," *Appl. Phys. Lett.*, vol. 92, no. 16, p. 162101, 2008.

[27] O. Madelung, *Semiconductors: Data Handbook*. Switzerland: Springer, 2012.

[28] R. Varache, J.-P. Kleider, M.-E. Gueunier-Farret, and L. Korte, "Silicon heterojunction solar cells: Optimization of emitter and contact properties from analytical calculation and numerical simulation," *Mater. Sci. Eng., B*, vol. 178, no. 9, pp. 593–598, 2013.

[29] J. Wang, F. Meng, Z. Fang, and Q. Ye, "Investigation of a-Si (N+)/c-Si (P) hetero-junction solar cell through AFORS-HET simulation," *Surf. Interface Anal.*, vol. 43, no. 9, pp. 1211–1217, 2011.

[30] H. Imran, T. M. Abdolkader, and N. Z. Butt, "Carrier-selective NiO/Si and TiO_2/Si contacts for silicon heterojunction solar cells," *IEEE Trans. Electron Devices*, vol. 63, no. 9, pp. 3584–3590, Sep. 2016.

[31] S. Nakano and Y. Takeuchi, "Experimental and simulation studies of interface properties of crystalline germanium heterojunction solar cells," in *Proc. IEEE Int. Nanoelectron. Conf.*, 2014, pp. 1–5.

[32] P. E. Blöchl, "Projector augmented-wave method," *Phys. Rev. B*, vol. 50, no. 24, p. 17953, 1994.

[33] G. Kresse and D. Joubert, "From ultrasoft pseudopotentials to the projector augmented-wave method," *Phys. Rev. B*, vol. 59, no. 3, pp. 1758–1775, 1999.

[34] G. Kresse and J. Hafner, "Ab initio molecular dynamics for liquid metals," *Phys. Rev. B*, vol. 47, no. 1, pp. 558–561, 1993.

[35] G. Kresse and J. Furthmüller, "Efficient iterative schemes for Ab initio total-energy calculations using a plane-wave basis set," *Phys. Rev. B*, vol. 54, no. 16, p. 11169, 1996.

[36] J. P. Perdew, K. Burke, and M. Ernzerhof, "Generalized gradient approximation made simple," *Phys. Rev. Lett.*, vol. 77, no. 18, p. 3865, 1996.

[37] A. Jain *et al.*, "Formation enthalpies by mixing GGA and GGA+ U calculations," *Phys. Rev. B*, vol. 84, no. 4, p. 045115, 2011.

[38] A. Schleife, F. Fuchs, C. Rödl, J. Furthmüller, and F. Bechstedt, "Branch-point energies and band discontinuities of III-nitrides and III-/II-oxides from quasiparticle band-structure calculations," *Appl. Phys. Lett.*, vol. 94, no. 1, p. 012104, 2009.

[39] L. Ward *et al.*, "Matminer: An open source toolkit for materials data mining," *Comput. Mater. Sci.*, vol. 152, pp. 60–69, 2018.

[40] R. Stangl, C. Leendertz, and J. Haschke, "Numerical simulation of solar cells and solar cell characterization methods: The open-source on demand program AFORS-HET," *Sol. Energy*, vol. 14, pp. 319–352, 2010.

[41] Y.-M. Lu, W.-S. Hwang, J. Yang, and H. Chuang, "Properties of nickel oxide thin films deposited by RF reactive magnetron sputtering," *Thin Solid Films*, vol. 420, pp. 54–61, 2002.

[42] I. Hotovỳ, J. Huran, J. Janik, and A. Kobzev, "Deposition and properties of nickel oxide films produced by DC reactive magnetron sputtering," *Vacuum*, vol. 51, no. 2, pp. 157–160, 1998.

[43] P. Salunkhe, M. A. AV, and D. Kekuda, "Investigation on tailoring physical properties of nickel oxide thin films grown by DC magnetron sputtering," *Mater. Res. Exp.*, vol. 7, no. 1, p. 016427, 2020.

[44] M. A. Leilaeioun, W. Weigand, M. Boccard, J. Y. Zhengshan, K. Fisher, and Z. C. Holman, "Contact resistivity of the p-type amorphous silicon hole contact in silicon heterojunction solar cells," *IEEE J. Photovol.*, vol. 10, no. 1, pp. 54–62, Jan. 2020.

[45] A. Jain *et al.*, "Commentary: The materials project: A materials genome approach to accelerating materials innovation," *APL Mater.*, vol. 1, no. 1, 2013, Art. no. 011002.

[46] W. Br *et al.*, "Stress development in sputtered NiO thin films during heat treatment," *J. Appl. Phys.*, vol. 94, no. 8, pp. 4853–4858, 2003.

[47] U. Rau and T. Kirchartz, "Charge carrier collection and contact selectivity in solar cells," *Adv. Mater. Interfaces*, vol. 6, no. 20, p. 1900252, 2019.

[48] P. Procel, G. Yang, O. Isabella, and M. Zeman, "Theoretical evaluation of contact stack for high efficiency IBC-SHJ solar cells," *Sol. Energy Mater. Sol. Cells*, vol. 186, pp. 66–77, 2018.

[49] W.-B. Zhang, N. Yu, W.-Y. Yu, and B.-Y. Tang, "Stability and magnetism of vacancy in NiO: A GGA+ U study," *Eur. Phys. J. B*, vol. 64, no. 2, pp. 153–158, 2008.

[50] M. Grilli *et al.*, "Effect of growth parameters on the properties of RF-sputtered highly conductive and transparent p-type NiO_x films," *Semicond. Sci. Technol.*, vol. 31, no. 5, p. 055016, 2016.

[51] J. Kim, Y. Ko, and K. Park, "Effect of RF magnetron sputtered nickel oxide thin films as an anode buffer layer in a P_3 HT: PCBM bulk hetero-junction solar cells," *Acta Phys. Polonica, A*, vol. 133, no. 4, pp. 887–891, 2018.

[52] H. Sun, S.-C. Chen, W.-C. Peng, C.-K. Wen, X. Wang, and T.-H. Chuang, "The influence of oxygen flow ratio on the optoelectronic properties of p-type $Ni_{1-x}O$ films deposited by ion beam assisted sputtering," *Coatings*, vol. 8, no. 5, p. 168, 2018.

[53] M. I. Pintor-Monroy, B. L. Murillo-Borjas, M. Catalano, and M. A. Quevedo-Lopez, "Controlling carrier type and concentration in NiO films to enable in situ PN homojunctions," *ACS Appl. Mater. Interfaces*, vol. 11, no. 30, pp. 27 048–27 056, 2019.

[54] J. Keraudy and P.-Y. Jouan, "Process-and optoelectronic-control of NiO_x thin films deposited by reactive high power impulse magnetron sputtering," *J. Appl. Phys.*, vol. 121, no. 17, p. 171916, 2017.

[55] J. Lee, A. Urban, X. Li, D. Su, G. Hautier, and G. Ceder, "Unlocking the potential of cation-disordered oxides for rechargeable lithium batteries," *Science*, vol. 343, no. 6170, pp. 519–522, 2014.

[56] R. Woods-Robinson, A. Fioretti, J. Haschke, K. Persson, M. Boccard, and C. Ballif, "Linking simulation and synthesis of nickel oxide hole-selective contacts for silicon heterojunction solar cells," in *Proc. IEEE 47nd Photovolt. Spec. Conf.*, 2020, pp. 1–5.

[57] R. Woods-Robinson *et al.*, "Wide band gap chalcogenide semiconductors," *Chem. Rev.*, vol. 120, pp. 4007–4055, 2020.

[58] W. D. Richards, L. J. Miara, Y. Wang, J. C. Kim, and G. Ceder, "Interface stability in solid-state batteries," *Chem. Mater.*, vol. 28, no. 1, pp. 266–273, 2015.

[59] K. Hubbard and D. Schlom, "Thermodynamic stability of binary oxides in contact with silicon," *J. Mater. Res.*, vol. 11, no. 11, pp. 2757–2776, 1996.

[60] A. Ringwood, "Prediction and confirmation of olivine–spinel transition in Ni_2SiO_4," *Geochimica et Cosmochimica Acta*, vol. 26, no. 4, pp. 457–469, 1962.

[61] R. Thompson, J. Angilello, and K.-N. Tu, "Crystallization kinetics of amorphous NiSix films," *Thin Solid Films*, vol. 188, no. 2, pp. 259–265, 1990.

[62] S. Zhong, J. Dreon, Q. Jeangros, E. Aydin, S. De Wolf, F. Fu, M. Boccard, and C. Ballif, "Mitigating plasmonic absorption losses at rear electrodes in high-efficiency silicon solar cells using dopant-free contact stacks," *Adv. Funct. Mater.*, vol. 30, no. 5, p. 1907840, 2020.

[63] G. Hautier, "Finding the needle in the haystack: Materials discovery and design through computational Ab initio high-throughput screening," *Comput. Mater. Sci.*, vol. 163, pp. 108–116, 2019.

[64] M. Chan and G. Ceder, "Efficient band gap prediction for solids," *Phys. Rev. Lett.*, vol. 105, no. 19, p. 196403, 2010.

[65] A. Goyal, P. Gorai, S. Anand, E. S. Toberer, G. J. Snyder, and V. Stevanović, "On the dopability of semiconductors and governing materials properties," *Chem. Mater.*, vol. 32, pp. 4467–4480, 2020.

[66] D. Broberg *et al.*, "PyCDT: A python toolkit for modeling point defects in semiconductors and insulators," *Comput. Phys. Commun.*, vol. 226, pp. 165–179, 2018. [Online]. Available: http://www.sciencedirect.com/science/article/pii/S0010465518300079

[67] C. A. Wolden *et al.*, "The roles of ZnTe buffer layers on CdTe solar cell performance," *Sol. Energy Mater. Sol. cells*, vol. 147, pp. 203–210, 2016.

[68] N. Sarmadian, R. Saniz, B. Partoens, and D. Lamoen, "Easily doped p-type, low hole effective mass, transparent oxides," *Sci. Rep.*, vol. 6, p. 20446, 2016.

[69] M. E. Levinshtein, S. L. Rumyantsev, and M. S. Shur, *Properties of Advanced Semiconductor Materials: GaN, AIN, InN, BN, SiC, SiGe*. New York, NY, USA: Wiley, 2001.